

Co-assembled Perylene/GO Photosensitive Heterobilayer for Efficient Neuromorphics

Heshan Zhang

Nanjing Tech University

Xue-Mei Dong

Nanjing Tech University

Zi-Cheng Zhang

Nanjing Tech University

Ze-Pu Zhang

Nanjing Tech University

Chaoyi Ban

Nanjing Tech University

Zhe Zhou

Nanjing Tech University

Cheng Song

Nanjing Tech University

Shiqi Yan

Nanjing Tech University

Qian Xin

Shandong University

Juqing Liu (✉ iamjqliu@njtech.edu.cn)

Nanjing Tech University <https://orcid.org/0000-0002-6499-2796>

Yin-Xiang Li

Nanjing Tech University

Wei Huang

Nanjing Technical University

Article

Keywords:

Posted Date: March 18th, 2022

DOI: <https://doi.org/10.21203/rs.3.rs-1461165/v1>

License:  This work is licensed under a Creative Commons Attribution 4.0 International License.

[Read Full License](#)

Version of Record: A version of this preprint was published at Nature Communications on August 25th, 2022. See the published version at <https://doi.org/10.1038/s41467-022-32725-y>.

Abstract

Neuromorphic electronics, which use artificial photosensitive synapses, can emulate biological nervous systems with in-memory sensing and computing abilities. Benefiting from multiple intra/interactions and strong light-matter coupling, two-dimensional heterostructures are promising synaptic materials for photonic synapses. Two primary strategies, including chemical vapor deposition and physical stacking, have been developed for layered heterostructures, but large-scale growth control over wet-chemical synthesis with comprehensive efficiency remains elusive. Here we demonstrate an interfacial coassembly heterobilayer films from perylene and graphene oxide (GO) precursors, which are spontaneously formed at the interface, with highly uniform bilayer structure of single-crystal perylene and well-stacked GO over centimeters in size. The planar heterostructure device exhibits an ultrahigh specific detectivity of 5.01×10^{16} Jones and ultralow energy consumption of 10^{-9} W as well as broadband photoperception from 365 to 1550 nm. Moreover, the device shows extraordinary photonic synaptic behaviors with a paired-pulse facilitation (PPF) index of 214% in neuroplasticity, and the heterosynapse array has the capability of information reinforcement learning and recognition.

Introduction

Layered heterostructures are promising neurotransmitters for artificial optoelectronic synapses due to their ultrasensitive light detection, tunable memory plasticity and ultralow energy potential^{1,2}. To achieve high-efficiency synaptic electronics, huge efforts have been made to construct versatile heterostructures and devices, especially low-dimensional (D) heterostructures from 0D-2D and 2D-2D combinations³. Among them, 2D heterostructures give more prominence to fascinatingly manipulating photogenerated excitons and charge transport at the interface^{4,5}. The coupling of light absorption regions of dissimilar layered matter allows wideband photodetection for the visual perception portion^{6,7}, and the unequal bandgaps and confinement transport enable optical memory plasticity for the information processing portion^{8,9}. Previous studies show that 2D photonic heterosynapses have a detection range from deep ultraviolet¹⁰ to the mid-infrared region¹¹, with specific detectivity up to 10^{16} Jones¹² and energy consumption as low as 10^{-9} W; however, their overall performance is not nearly as good as that of a biological synapse^{13,14}.

Conventional layered heterostructure assembly relies mainly on physical stacking and chemical vapor deposition technologies. Several inorganic bilayer heterostructures, including $\text{WSe}_2\text{-MoS}_2$ ¹⁵, $\text{WSe}_2\text{-SnS}_2$ ¹⁶, and GaTe-MoS_2 ¹⁷, have been successfully constructed. However, there are still a few imperfections in the resulting materials, such as grain boundaries with weak homogeneity¹⁸, unscalable exfoliation with inefficient transfer¹⁹, and complicated processes with high expense. Furthermore, the relatively high mobility of inorganic layered crystals ($100 \text{ cm}^2 \text{ V}^{-1} \text{ s}^{-1}$) normally accompanies a relatively high dark current and operating current simultaneously, thus making it hard to enhance the specific detectivity and reduce the power dissipation in man-made synapses, all of which limit the practicality of

monolithically large-scale manufacturing and competitive applications. In contrast, carbon-based compounds, especially aromatic-containing organic and graphene oxide (GO), are promising candidates for efficient synapses in neuromorphic electronics, because of tailored chemical structures, tunable photoelectric properties, and facile solution processes¹³. Moreover, these compounds can be assembled into a variety of nanostructures with fascinating features mostly derived from van der Waals (vdW), electrostatic adherence, and supramolecular as well as cooperative interactions²⁰. Herein, we report an interfacial coassembly approach to prepare a centimeter-size and uniform photosensitive heterobilayer from perylene and GO precursors, and then utilize the heterobilayer to construct high-performance photo perception and synaptic plasticity with broadband sensitivity, ultralow power, ultrahigh specific detectivity, and ultrahigh learning efficiency.

Results And Discussion

Perylene/GO heterobilayer coassembly and characteristics. **Figure 1a** schematically illustrates the interfacial assembly of the bilayer heterostructure from perylene and GO precursors. Perylene can act as a semiconductor building block to assemble a crystalline layer at the gas-liquid interface with broadband absorption in the visible region^{21, 22} due to the relatively strong π - π interactions of aromatic-rich frameworks. GO sheet, as graphene-like aromatic patch, has versatile decoration of polar oxygen-containing hydrophilic groups, such as $-OH$, $=O$, and $-COOH$, which can not only endow GO self-assembly or coassembly with other materials, including aromatic complexes but also enable light overlapping absorption in the visible to ultraviolet (UV) and near-infrared (NIR) regions for perylene/GO hybridization. According to the step-by-step guideline (**Figure S1**), the GO solution in methanol was first dropped onto the water, and subsequently, the perylene/toluene solution was dropped onto the GO solution. The polar groups of GO can reduce the interfacial tension at the liquid-liquid interface, thus enhancing the spreading of the perylene solution and fully covering the water surface. Under the driving of vdW forces between precursor matter, GO self-assembly and GO-guided perylene assembly simultaneously occur at the interface, resulting in the formation of a continuous centimeter-sized thin film with a homogeneous color distribution over a region of $1.5\text{ cm} \times 1.5\text{ cm}$ (**Figure 1b**), indicating the uniform and scalable growth of such heterostructures. As shown in **Figure S2a**, only small-size ($50\text{ }\mu\text{m}$) and crackable perylene crystals were achieved under the identical procedure without the addition of GO, suggesting that GO plays a critical role in large-area assembly of perylene. Moreover, by modulating the injected volume or concentration of GO solution, layer thickness at the nanoscale level can be realized from 40 to 160 nm (**Figure S3**), following a linear progression with volume. Our method paves the way for the assembly synthesis of large-area carbon-rich heterostructures.

To preliminarily investigate the morphology and structure of the assembled heterostructure, two films were directly transferred onto $300\text{ nm SiO}_2/\text{Si}$ substrates with front and reverse side contacts. The atomic force microscopy (AFM) images in **Figures 1c, d** show that the film has a smooth upper surface and coarse bottom surface that contain discrete nanosheets, with roughness of 0.62 nm and 5.58 nm, respectively. Compared with the wrinkled-like surface of the pure GO film (**Figure S4**), we speculate that

the discrete matter on the bottom surface is GO sheets, while the smooth layer should consist of perylene. The GO sheets are stacked into a paper-like membrane that contacts the perylene layer, suggesting layer-by-layer assembly of the heterostructure. **Figures 1e, f** explain the integrality and crystal characteristics of the perylene layer by using an optical microscope with cross-polarized detection. The color change on the surface is uniform and significant after a 45 degrees rotation²³, revealing its monolithic single-crystal nature.

To further evaluate the film quality and chemical components, the heterostructure was transferred onto a SiO₂/Si substrate with the GO layer in contact with air. The optical image presents homogeneous contrast over a region of 500×375 μm (**Figure 2a**), confirming the uniform and scalable growth of such heterostructure. By extracting and comparing five Raman spectra from variable regions in the mapping area, four-mode absorption and negligible variation in each region are summarized (**Figure 2b, c**). The two relatively weak peaks of 1296 cm⁻¹ and 1366 cm⁻¹ could be ascribed to the characteristic peaks of the crystalline perylene layer²⁴, and the two strong peaks at 1332 cm⁻¹ and 1583 cm⁻¹ are identified as the D-band and G-band of the well-stack GO layer^{25, 26}, respectively (**Figure S5**). This result verifies the growth uniformity and chemical constitution of perylene and GO in our large-scale heterostructure. Moreover, the atomic composition in each region was analyzed by energy-dispersive X-ray spectroscopy (EDS). As shown in **Figure S6**, the bottom layer mainly contains signals of carbon (C, yellow) and oxygen (O, red) elements from GO matter, and the C atomic signals in the upper layer are derived from perylene molecules.

The detailed crystal structure of the obtained heterostructure was symmetrically assessed by X-ray powder diffraction (XRD), selected area electron diffraction (SAED) and cross-sectional scanning transmission electron microscopy (STEM). In XRD, the diffraction peak at 2θ = 18° is assigned to the (002) diffraction pattern for perylene (**Figure S8**), manifesting the *ab* plane of the crystal film parallel to the substrate. All characteristic peaks of the perylene crystal and GO layer (2θ = 14° and 17°) appear without any unidentified peaks (**Figure 2d**), suggesting that no new phase formed in the coassembly process. This conclusion can be further confirmed by the SAED of perylene crystals exfoliated from the heterostructure (**Figure 2e**). The remarkable bright spots in SAED, with the largest crystal face of (002), match well with the above XRD result of perylene. From the cross-section image of the bilayer heterostructure measured by STEM, the thickness of GO layer is approximately 3 nm (**Figure 2f**).

Based on the above analysis, the inner molecular packing of the heterostructure is presented in **Figure 2g** and **Figure S9**. The crystalline perylene adopts herringbone-like packing, with a strong π–π partial overlap of 3.481 Å between adjacent molecules in the *ab* plane, resulting in parallel stacking to the surface of the GO layer. In this stacking, the molecular long axis of perylene was tilted by 45° with respect to the crystallographic *c*-axis, leading to strong π–π stacking interaction between perylene and GO. In particular, multiple hydrogen bond interactions, such as C=O···H and O–H···H, may also exist between multiple oxygen-containing groups of GO and the edge face of perylene. The abundant π···π stacking/hydrogen bond interactions can form a 2D network of intermolecular forces, which reduce the

nucleation energy of precursors for efficient 2D assembly and also afford strong cohesion between the two layers within the heterostructure. Such advances in combining two matters and abundant interactions endow the hybrid with strong light-matter coupling and ultrabroadband light absorption from UV to visible/NIR regions compared to each single-component (**Figure S10**), which are suitable for high-performance optoelectronics.

Photosensitive characteristics. As discussed above, we have achieved a high-quality large-area perylene/GO heterobilayer. To explore the physical properties, we assembled a 40 nm thick heterostructure film and studied the photoelectric effect of this film. **Figure 3a** shows the configuration of the in-plane heterostructure device and its corresponding band diagram. Since graphene has atomically electroactive surface, its Fermi level can be tuned by heteroatom doping or environmental change, making it promising for versatile detection.²⁷ Oxygen decoration as an electron acceptor normally leads to p-type doping and induces abundant defects in GO, with an average energy level of 4.9 eV measured by an ultraviolet photoelectron spectrometer (UPS) (**Figure S12**), which provides hole transport pathways for carbon electronics. Under illumination, the heterostructure absorbs light energy to generate electron-hole pairs, and these photo excited electrons at the interface are trapped within defect sites, while holes transport along the pathways, thus producing a photoresponse current^{12, 28-30}.

The heterostructure device exhibits wide-band photoperception abilities (365-1550 nm, **Figure 3b, Figure S13**) due to the synergic light absorption of perylene and GO. The photoresponsivity (R , defined by I_{ph}/P) as a function of wavelength is depicted to examine the photoelectric conversion performance (**Figure 3c, Figure S14**), where I_{ph} is the photocurrent and P is the power of incident light. Interestingly, the detector has a normal distribution of photosensitivity within the visual range, with the highest photoelectric conversion efficiency of approximately 500 nm. This trend is analogous to the retina-like photoperception function for biomimetic eyes^{31, 32}.

To gain more insight into the photodetector performance, the impact of incident light power on the photoresponsivity at different excitation wavelengths was studied. In the visible region at 530 nm, the device exhibits the highest responsivity of 110 mA W⁻¹ at an excitation power of 0.01 μW, indicating its outstanding ability for weak light detection. However, the responsivities in the UV and NIR regions are relatively low, with values of 30 and 24 mA W⁻¹, respectively (**Figure 3d**). **Figure 3e** illustrates the power-dependent photoresponse under 530 nm light illumination. The photocurrent has a positive nonlinear relation with the power intensity, while the corresponding responsivity decreases exponentially. With the increase of power, more photoexcited carriers will generate and contribute to a higher electric field with an opposite built-in field in the junction, which can hinder the separation of more electron-hole pairs, thus present a smaller responsivity^{28, 30, 33}. Importantly, the photodetector shows excellent repeatability and stability of the photoelectric switch (**Figure 3f, Figure S15**). Based on the rising and falling steps of the time-resolved photo response curves, the rise time (τ_r) and fall time (τ_f), defined as the time required for photocurrent rise/drop between 10% and 90%, are 50 ms and 3 s, respectively (**Figures 3g, h**). The slow τ_f

is probably attributed to the decay of persistent photocurrent induced by excess electrons trapped in GO defects, which makes the heterostructure a promising synapse for neuromorphic electronics.

As a figure of merit, the specific detectivity D^* is widely used to assess the detection capability of photodetectors. Theoretically, D^* is derived from the noise equivalent power (NEP), detector area (A) and detection bandwidth (Δf), which can be calculated using the following equation:

$$D^* = \frac{\sqrt{A \Delta f}}{NEP} = \frac{R_i}{I_d} \sqrt{A \Delta f} \quad (1)$$

where I_d is the dark current, R_i is the photoresponsivity, and NEP is defined as the ratio of I_d/R_i . Due to the relatively low conductivity of GO matter³⁴, the dark current of our device is as low as 1 pA (**Figure 3b, Figure S16**). Together with its high photoresponsivity (110 mA W⁻¹) at 530 nm, the detector has an ultrahigh D^* of 5.01×10¹⁶ Jones. Moreover, the photodetector shows an ultralow operating power of 10⁻⁹ W. **Figure 3i** summarizes the D^* and power consumption P of emerging photodetectors based on GO/perylene and some previously reported heterostructures. Impressively, our GO/perylene detector possesses the highest D^* and lowest P among all these devices (**Table S1**). It is concluded that emerging 2D heterostructures are more competitive than most traditional heterojunctions in the biomimetic retina for light detection.

Photonic synaptic characteristics. The obtained detector has wideband light perception, slows signal decay, ultrahigh specific detectivity, and ultralow energy consumption, which endow the device to emulate visual perception and synaptic plasticity, such as biological neurons, with the characteristics of an excitatory postsynaptic current (EPSC), spike-intensity dependent plasticity (SIDP), spike-number dependent plasticity (SNDP), paired-pulse facilitation (PPF), short-term memory (STM), and long-term memory (LTM)^{35, 36}. With a single UV pulse (0.144 μW mm⁻², 15 s) under 1 V, a large number of photogenerated carriers are generated and transferred from perylene to GO, resulting in a surge of EPSC (**Figure S17**). After switching off the light, the photocurrent declines with a long-term relaxation process due to the slow release of trapped carriers in defects. **Figure S18** demonstrates the EPSC of two successive weak light pulses (0.144 μW mm⁻², Δt = 2 s). The current peak from the second pulse (A_2) is higher than that from the first pulse (A_1), and the ratio A_2/A_1 is called PPF³⁷. In biology, PPF is a critical short-term plasticity enhancement process and is essential for the temporal decoding of visual signals^{38, 39}.

Notably, the artificial heterosynapse shows evident PPF behavior during successfully pulsed light with ultrabroadband wavelengths from UV to NIR (**Figure 4a**). Both SIDP and SNDP behaviors were investigated in **Figures 4b, c**. The overall EPSC is proportional to light intensity and pulse number, and the refresh signal after receiving the latter pulse is higher than that after receiving the former pulse, indicating synaptic plasticity enhancement by raising learning intensity and times. This enhancement is probably attributed to the superposition of subsequent excited carriers with partial carriers left before the following

pulse, because of efficient generation and slow decay of carriers under short pulse interval^{40, 41}. To quantify the PPF, the amplitudes of the postsynaptic current under multiple pulses are calculated in **Figures 4d, e**, where the A_n/A_1 index is denoted as the ratio of the first and last spike currents. With the increase in pulse number, the growth rates of amplitude amplification slow until approaching a saturation state (209.9%). **Figure 4f** explores spike-time-interval-dependent (STIDP) plasticity with variable intervals ranging from 0.1 to 30.0 s. The index progressively declines with increasing interval, and this attenuation curve matches well with the double exponential function, showing a great ability to mimic biological PPF behavior³⁷. The photonic synapse has a maximum PPF up to 214%, the value exceeds the best performance of synapses from 2D heterostructures (**Table S2**), meaning an outstanding learning efficiency.

According to Ebbinghaus's theory⁴², relearning information in biological synapses takes less time than initial learning. To emulate this learning-experience behavior, the device was irradiated by two adjacent 365 nm light pulses with identical intensities ($0.432 \mu\text{W mm}^{-2}$) and tunable intervals. As shown in **Figure 4g**, it takes 21.0 s to reach the 214 pA level during the original learning, and then the recorded signal decays exponentially. In contrast, subsequent learning only requires 10.2 s to approach the same cognitive level, which is similar to human-like learning⁴³. Furthermore, the transition from the STP to LTP process is described in **Figure 4h**. By applying two successive pulses with a pulse frequency of 1 Hz, a pulse width of 0.5 s, and a pulse intensity of $0.144 \mu\text{W mm}^{-2}$, the memory strength of the signal declines rapidly to 40 pA in a short interval of 30 s, which is defined as the STP process. When 13 successive pulses are applied, the signal descending to the reference level requires a longer decay time of 160 s, resulting in the formation of LTP. Therefore, the STP can be progressively converted to LTP by modulating the number of pulse learning⁴⁴.

The outstanding learnability enables artificial synapses to mimic visual learning for high-quality image sensing and deep learning. To this end, a random pattern image "CEO" as signal input consists of 10×10 synapse pixels, and the gray of each pixel represents the measured ESPC value. **Figure 5a** illustrates the evolution of pixel gray over pulse times in the mapping area simulated by synapse arrays. After applying the training of 0, 5, 7, 9, 11 and 13 pulse spikes with a weak (0.288 W mm^{-2}) light, the weighted graphs of learning patterns have enhanced sharpness and likeness to these input letters. As the pulse number reaches a certain level, the distinct target image becomes uniform and easily recognizable. Furthermore, to assess the memory effect under variable learning intensity, we investigated the influence of illumination intensity on pixel gray (current) under 9 fixed pulses at 365 nm light. As the intensity of learning increases to $0.72 \mu\text{W mm}^{-2}$, a clear shape of the "CEO" figure was also achieved (**Figure 5b**), meaning that the efficiency of visual learning can be accelerated by enhancing light intensity. These features are analogous to the image learning of biological neurons.

To assess the reliability of our photonic synapse in image cognition, the accuracy of an artificial neural network (ANN) is simulated and calculated by utilizing the heterosynapse as a neuron. In biological neural networks, both LTP and short-term depression (LTD) processes are required to depolarize and

reverse neurons, respectively, which can dynamically balance the synaptic weight for efficient signal processing⁴⁵. The constructed heterosynapse not only has an LTP feature but also possesses LTD behavior under the unipolar pulsed bias (**Figure S18**). Their corresponding nonlinearities as learning efficiency and recognition rates are extracted by fitting the experimental data, with a maximum value of 1.98 for LTP and 4.21 for LTD (**Figure S19**). This bidirectional modulated function with appropriate nonlinearity allows them to construct an efficient ANN⁴⁶.

Figure 5c depicts the schematic light-derived ANN architecture comprising 784 inputs, 2 hidden and 10 outputs. A 28×28 handwritten pattern recognition was adopted from the database of the Modified National Institute of Standards and Technology⁴⁷, with one photonic synapse at each intersection of the crossbar structure (**Figure S20**). According to the above model, the accuracy of recognition was calculated by using 60000 training and 10000 test images as well as 64 batch sizes at each epoch. In contrast to unidirectional modulation, the bidirectional strategy shows a higher accuracy of 85% (**Figure S21**), indicating advanced cognitive capability for more complex neuromorphic information. **Figure 5d** demonstrates the high dependence of cognitive accuracy on epochs under different pulse times. The overall accuracy for all pulse states improves at a faster rate during the initial epoch, and then tends to saturate at approximately 15 epochs. As the number of pulses increases from 3 to 8 and 13 times, the responding saturated accuracy increases from 50% to 60% and 80%, respectively. The results were clarified by simulating number "7" along with the evolution of learning stages (**Figure S22**).

In summary, we demonstrated a facile interfacial coassembly of a large-area photosensitive heterobilayer and utilized it as an optoelectronic converter for efficient neuromorphic electronics. The heterobilayer was assembled from GO and perylene at the liquid–liquid interface, with the merits of centimeter-scale, high uniformity and broadband absorption from visible to NIR regions. These characters ensure the exceptional photoperception of planar heterostructure devices, with an ultrahigh detectivity of 5.01×10^{16} Jones, ultralow power consumption of 10^{-9} W, and typical photonic synaptic behaviors, including EPSC, SIDP, SNDR, PPF, STP, LTP, and LTD under appropriate light and electrical pulses, which can serve as bioinspired photoreceptors and synapses synchronously. Specifically, this heterosynapse as an artificial neuron can be implemented into a neuromorphic network that is capable of visual learning and recognition. Our work provides an effective strategy for wafer-scale production of economical low-dimensional heterostructures for bioinspired optoelectronics.

Declarations

Supporting Information

Experimental details. Characterization techniques and additional data and results. These materials are available free of charge.

ACKNOWLEDGMENTS

The authors acknowledge the financial support from the National Key R&D Program of China (2017YFB1002900), the National Natural Science Foundation of China (61622402, 62104104), the China Postdoctoral Science Foundation (2020M671459), and the Jiangsu Specially Appointed Professor program.

NOTES

The authors declare no competing financial interest.

AUTHOR CONTRIBUTIONS

W.H., J.L., H. Z and X.D. conceived and designed the project. W.H. and J.L. supervised the project. H.Z., X.D., Y.L., Z.Z., C.S., J.L. and W.H. performed the experiments, including both fabrication and characterization. X.D. and Y.L. obtained the heterostructure and analyzed the data. H.Z. and X.D. performed the photoelectric measurements of the heterostructure device. C.B. assisted in the optoelectronic measurements. H.Z. and Z.Z. implemented the neural network. S.Y. and Q.X. were responsible for the TEM and SEM characterization. H.Z. and X.D. wrote the paper. J.L., Y.L. and Z.Z. revised the manuscript and provided some suggestions. All the authors discussed the results and commented on the manuscript.

References

1. Feldmann J., Youngblood N., Wright C. D., Bhaskaran H. & Pernice W. H. P. All-optical spiking neurosynaptic networks with self-learning capabilities. *Nature* **569**, 208–214 (2019).
2. Shastri B. J. et al. Photonics for artificial intelligence and neuromorphic computing. *Nat. Photonics* **15**, 102–114 (2021).
3. Liu Y. et al. van der Waals heterostructures and devices. *Nat. Rev. Mater.* **1**, 1–17 (2016).
4. Britnell L. et al. Electron tunneling through ultrathin boron nitride crystalline barriers. *Nano Lett.* **12**, 1707–1710 (2012).
5. Withers F. et al. Light-emitting diodes by band-structure engineering in van der Waals heterostructures. *Nat. Mater.* **14**, 301–306 (2015).
6. Koppens F. H. et al. Photodetectors based on graphene, other two-dimensional materials and hybrid systems. *Nat. Nanotechnol.* **9**, 780–793 (2014).
7. Saran R. & Curry R. J. Lead sulphide nanocrystal photodetector technologies. *Nat. Photonics* **10**, 81–92 (2016).
8. Sangwan V. K. & Hersam M. C. Neuromorphic nanoelectronic materials. *Nat. Nanotechnol.* **15**, 517–528 (2020).
9. Meng Y., Li F., Lan C., Bu X. & Ho J. C. Artificial visual systems enabled by quasi-two-dimensional electron gases in oxide superlattice nanowires. *Sci. Adv.* **6**, eabc6389 (2020).

10. Zhou F. et al. Optoelectronic resistive random access memory for neuromorphic vision sensors. *Nat. Nanotechnol.* **14**, 776–782 (2019).
11. Feng G. et al. Flexible Vertical Photogating Transistor Network with an Ultrashort Channel for In-Sensor Visual Nociceptor. *Adv. Funct. Mater.* **31**, (2021).
12. Zhu Q. B. et al. A flexible ultrasensitive optoelectronic sensor array for neuromorphic vision systems. *Nat. Commun.* **12**, 1798 (2021).
13. Lee Y., Park H.-L., Kim Y. & Lee T.-W. Organic electronic synapses with low energy consumption. *Joule* **5**, 794–810 (2021).
14. Mennel L., Symonowicz J., Wachter S., Polyushkin D. K. & Mueller T. Ultrafast machine vision with 2D material neural network image sensors. *Nature* **579**, 62–66 (2020).
15. Huo N. et al. Novel and Enhanced Optoelectronic Performances of Multilayer MoS₂-WS₂Heterostructure Transistors. *Adv. Funct. Mater.* **24**, 7025–7031 (2014).
16. Zhou X. et al. Tunneling Diode Based on WSe₂/SnS₂ Heterostructure Incorporating High Detectivity and Responsivity. *Adv. Mater.* **30**, (2018).
17. Wang F. et al. Tunable GaTe-MoS₂ van der Waals p-n Junctions with Novel Optoelectronic Performance. *Nano Lett.* **15**, 7558–7566 (2015).
18. Zhao B. et al. High-order superlattices by rolling up van der Waals heterostructures. *Nature* **591**, 385–390 (2021).
19. Schranghamer T. F., Sharma M., Singh R. & Das S. Review and comparison of layer transfer methods for two-dimensional materials for emerging applications. *Chem. Soc. Rev.* **50**, (2021).
20. Shao J. J., Lv W. & Yang Q. H. J. A. M. Self-assembly of graphene oxide at interfaces. **26**, 5586–5612 (2014).
21. Qian J. et al. Solution-processed 2D molecular crystals: fabrication techniques, transistor applications, and physics. *Adv. Mater. Technol.* **4**, 1800182 (2019).
22. Li Z. Z., Liao L. S. & Wang X. D. Controllable synthesis of organic microcrystals with tunable emission color and morphology based on molecular packing mode. *Small* **14**, 1702952 (2018).
23. Li Y. X. et al. A Bio-Inspired Molecular Design Strategy toward 2D Organic Semiconductor Crystals with Superior Integrated Optoelectronic Properties. *Small* **17**, 2102060 (2021).
24. Loppnow G. et al. UV Raman spectroscopy of hydrocarbons. *Philos. Trans. R. Soc., A* **362**, 2461–2476 (2004).
25. Girish C. M., Sasidharan A., Gowd G. S., Nair S. & Koyakutty M. Confocal Raman imaging study showing macrophage mediated biodegradation of graphene in vivo. *Adv. Healthcare Mater.* **2**, 1489–1500 (2013).
26. Peng G. et al. Nitric oxide-dependent biodegradation of graphene oxide reduces inflammation in the gastrointestinal tract. *Nanoscale* **12**, 16730–16737 (2020).
27. Chang H. et al. Thin Film Field-Effect Phototransistors from Bandgap-Tunable, Solution-Processed, Few-Layer Reduced Graphene Oxide Films. *Adv. Mater.* **22**, 4872–4876 (2010).

28. Liu C. H., Chang Y. C., Norris T. B. & Zhong Z. Graphene photodetectors with ultra-broadband/ultrabroadband and high responsivity at room temperature. *Nat. Nanotechnol.* **9**, 273–278 (2014).
29. Kim M. K. & Lee J. S. Synergistic Improvement of Long-Term Plasticity in Photonic Synapses Using Ferroelectric Polarization in Hafnia-Based Oxide-Semiconductor Transistors. *Adv. Mater.* **32**, e1907826 (2020).
30. Liu J. et al. Hole and electron extraction layers based on graphene oxide derivatives for high-performance bulk heterojunction solar cells. *Adv. Mater.* **24**, 2228–2233 (2012).
31. Wyszecki G. *Color science: concepts and methods, quantitative data and formulae / Gunter Wyszecki, W. S. Stiles*, 2000.
32. Poynton C. *Digital Video and HD*, 2012.
33. Konstantatos G., Badioli M., Gaudreau L., Osmond J. & Koppens F. H. L. Hybrid graphene–quantum dot phototransistors with ultrahigh gain. *Nat. Nanotechnol.* **7**, 363–368 (2012).
34. Lei D., Yang J., Chhowalla M. & Loh K. P. Synthesis and reduction of large sized graphene oxide sheets. *Chem. Soc. Rev.* **46**, (2017).
35. Strukov D. B., Snider G. S., Stewart D. R. & Williams R. S. The missing memristor found. *Nature* (2008).
36. Hu S. G. et al. Emulating the paired-pulse facilitation of a biological synapse with a NiOx-based memristor. *Appl. Phys. Lett.* **102**, 649 (2013).
37. Schulz P. E., Cook E. P. & Johnston D. Changes in paired-pulse facilitation suggest presynaptic involvement in long-term potentiation. *J. Neurosci.* **14**, 5325–5337 (1994).
38. Abbott L. F. & Regehr W. G. Synaptic computation. *Nature* **431**, 796–803 (2004).
39. Yang Y., He Y., Nie S., Shi Y. & Wan Q. Light Stimulated IGZO-Based Electric-Double-Layer Transistors For Photoelectric Neuromorphic Devices. *IEEE Electron Device Lett.* 1–1 (2018).
40. Liu C., Chen H., Wang S., Liu Q. & Zhou P. Two-dimensional materials for next-generation computing technologies. *Nat. Nanotechnol.* **15**, 545–557 (2020).
41. Wei S., Wang F., Zou X., Wang L. & Liao L. Flexible Quasi-2D Perovskite/IGZO Phototransistors for Ultrasensitive and Broadband Photodetection. *Adv. Mater.* 1907527 (2020).
42. Underwood & Benton J. Interference and forgetting. *Psychol. Rev.* **64**, 49–60 (1957).
43. Wang Z. Q. et al. Synaptic learning and memory functions achieved using oxygen ion migration/diffusion in an amorphous InGaZnO memristor. *Adv. Funct. Mater.* **22**, 2759–2765 (2012).
44. Wang X. et al. Highly sensitive artificial visual array using transistors based on porphyrins and semiconductors. *Small* **17**, 2005491 (2021).
45. Stanton P. K. LTD, LTP, and the sliding threshold for long-term synaptic plasticity. *Hippocampus* **6**, 35–42 (1996).
46. Choi Y., Oh S., Qian C., Park J.-H. & Cho J. H. Vertical organic synapse expandable to 3D crossbar array. *Nat. Commun.* **11**, 1–9 (2020).

47. LeCun Y., Bottou L., Bengio Y. & Haffner P. Gradient-based learning applied to document recognition. *Proc. IEEE* **86**, 2278–2324 (1998).

Figures

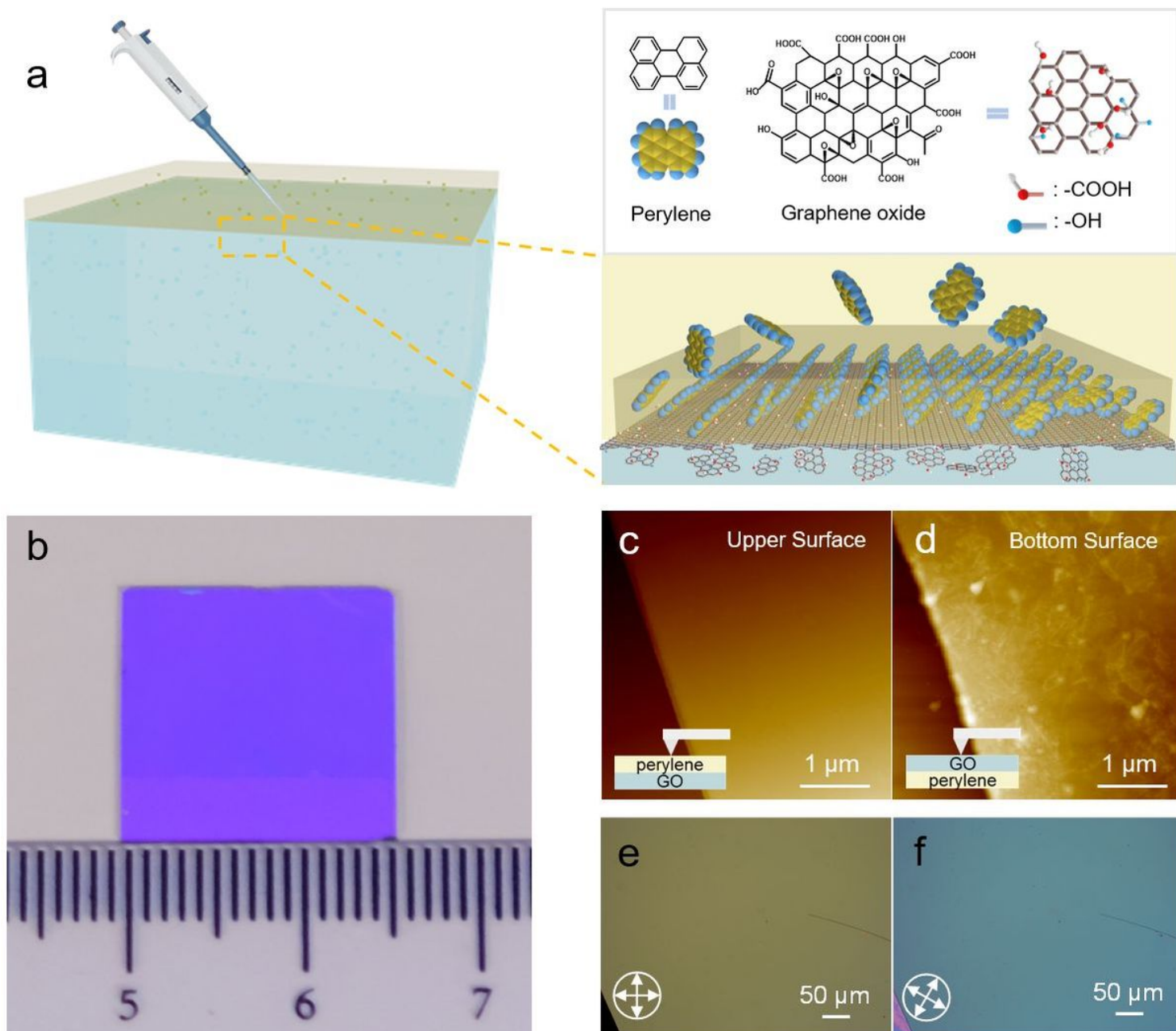


Figure 1

Coassembly and morphology of bilayer heterostructure. a) Schematic illustration of the coassembly of GO and perylene at the interface. b) Photograph of the assembled film on a SiO₂/Si substrate under daylight. AFM images of c) the upper surface and d) the bottom surface of the film. e, f) Polarization optical microscope images of the upper layer from the heterostructure.

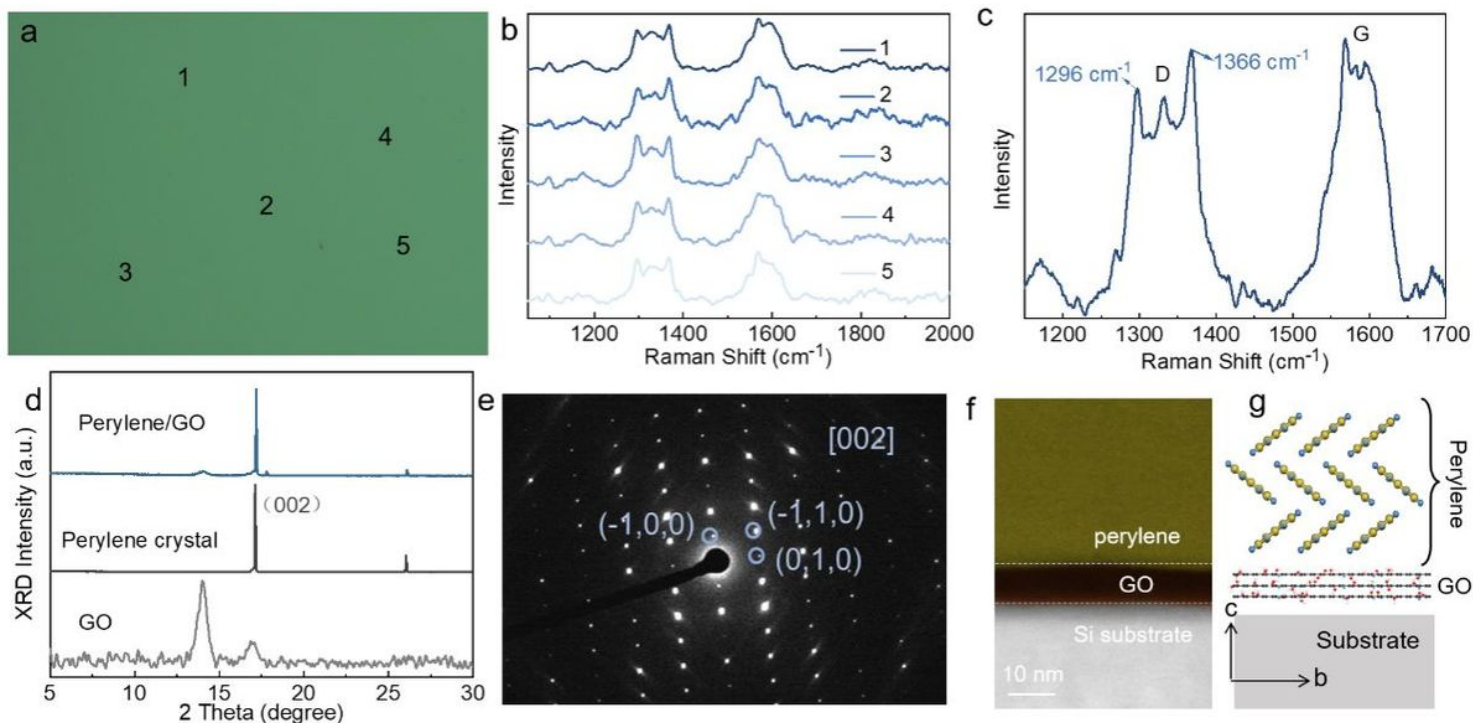


Figure 2

Structural characterization of the perylene/GO heterobilayer. a) Optical image of the heterostructure film transferred onto a 300-nm SiO₂/Si wafer. b) Raman spectra collected from regions labeled 1–5 in 2a. c) Zoomed-in view of Raman spectra with four mode absorption. d) XRD spectra taken from GO, perylene crystals and their combination. e) SAED image of perylene crystal. f) Cross-section STEM image of the bilayer perylene/GO structure on a silicon holder. g) Ordered molecular arrangement of perylene crystal viewed from the *b* axis of the lattice and GO layer; yellow, carbon atom; blue, hydrogen atom.

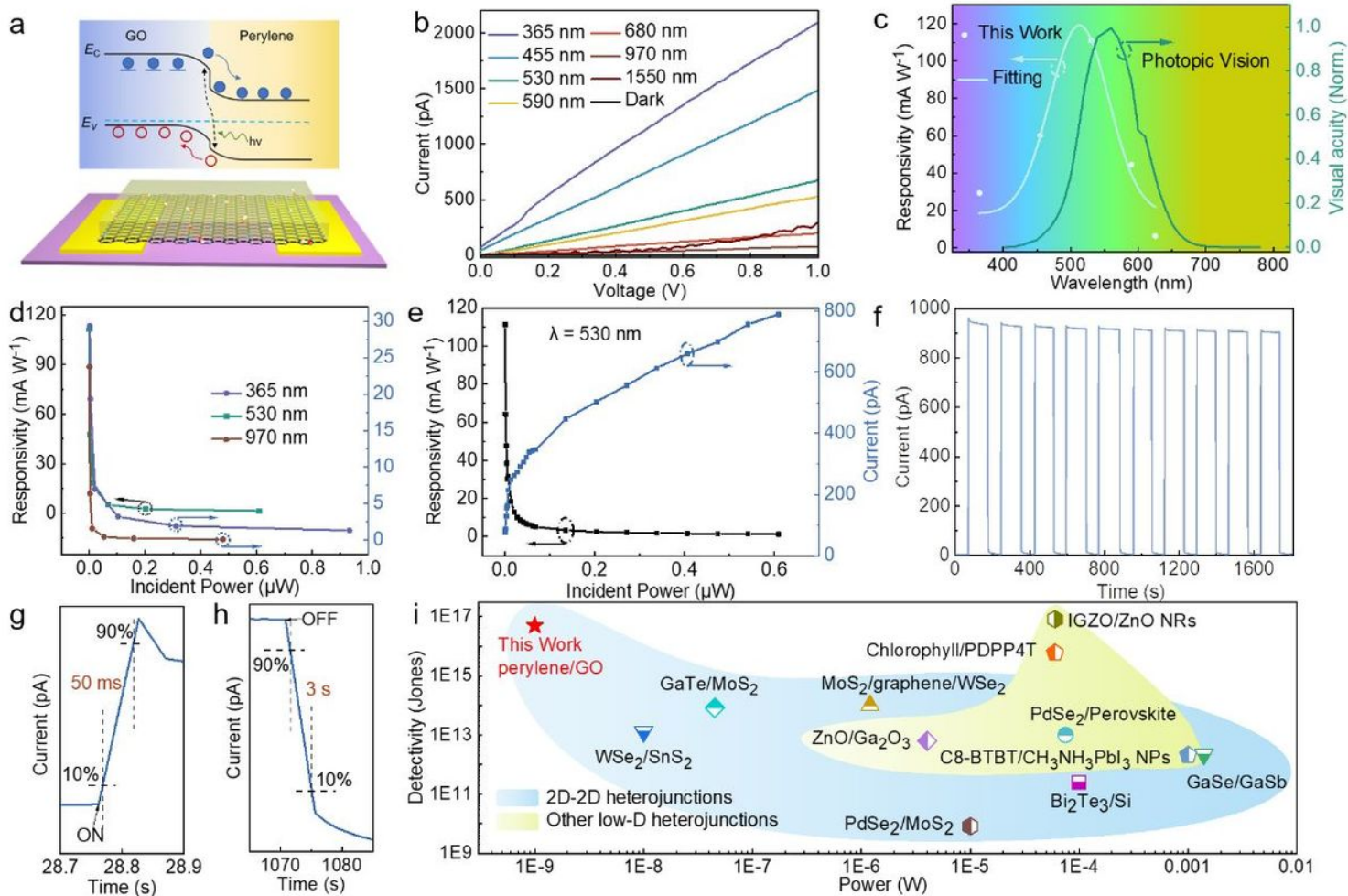


Figure 3

Perylene/GO heterobilayer photodetector. a) Structural scheme and energy band diagram of the in-plane heterostructure device. b) Photoresponse behaviors under UV, visible and NIR light stimuli. c) Visual sensitivity of the human eye and visible light responsiveness of the detector. d) Photoresponsivity as a function of incident light power at 365, 530, and 970 nm. e) Dependence of photocurrent and photoresponsivity on incident power at 530 nm. f) Time-resolved photocurrent of the detector excited at 365 nm. g, h) The rise and fall relaxation time of the photocurrent. i) Comparison of specific detection rate and power consumption of heterostructure photodetectors in the previous literature.

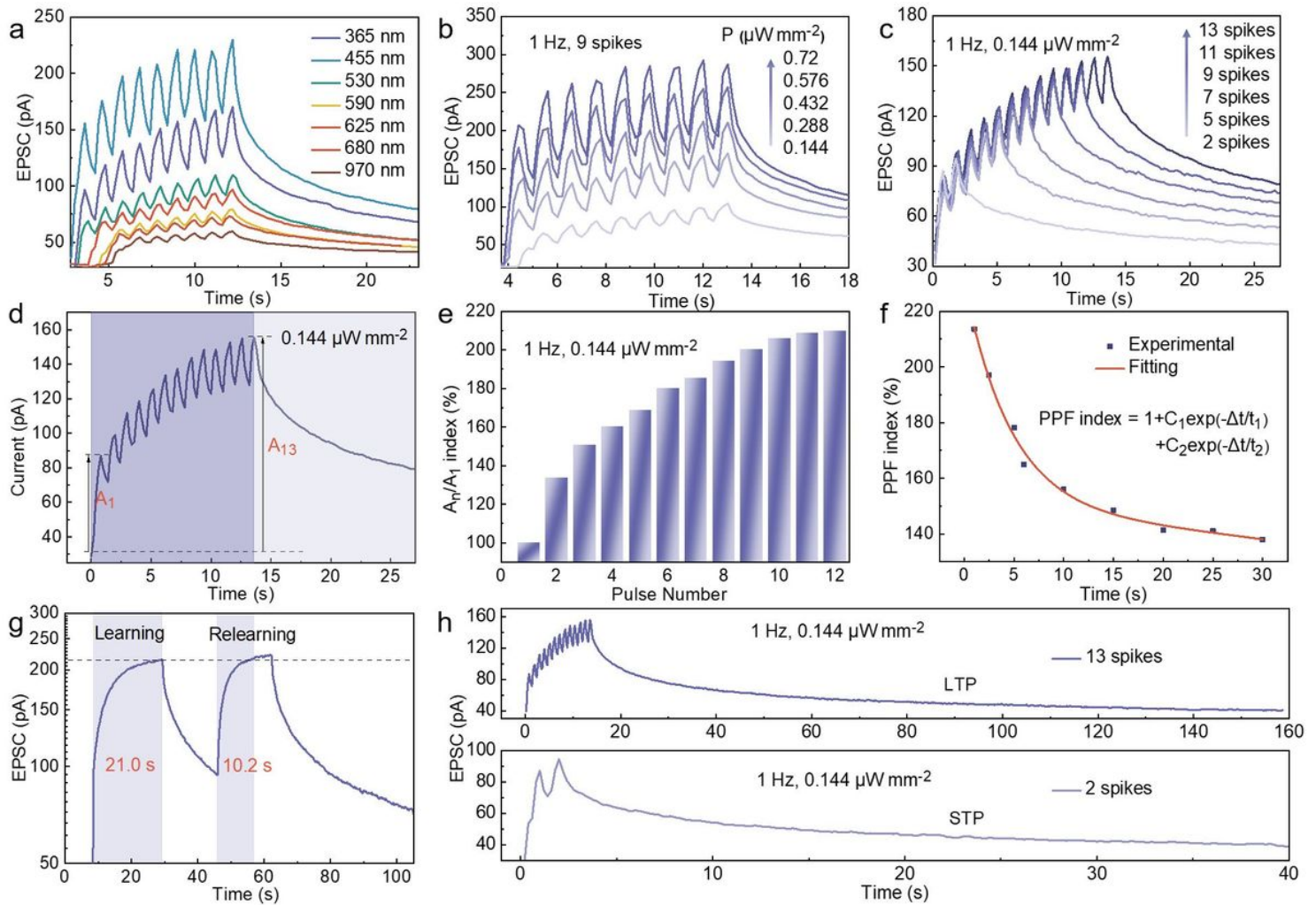


Figure 4

Phototunable synaptic properties. EPSCs in response to 9 successive light pulses a) under UV, visible and infrared light sources and b) under different powers with a fixed wavelength at 365 nm and a frequency of 1 Hz. c) Influence of the pulse number on EPSCs under fixed power at 365 nm ($0.144 \mu\text{W mm}^{-2}$, 1 Hz). d) Measured photocurrent generated by multiple light pulses and the definition of the index (A_{13}/A_1). e) The evolution of the A_n/A_1 index with the pulse number. f) PPF index plotted as a function of interspike interval. g) The learning-experience behavior of the photonic synapse device. h) STP and LTP processes under 2 and 13 pulses.

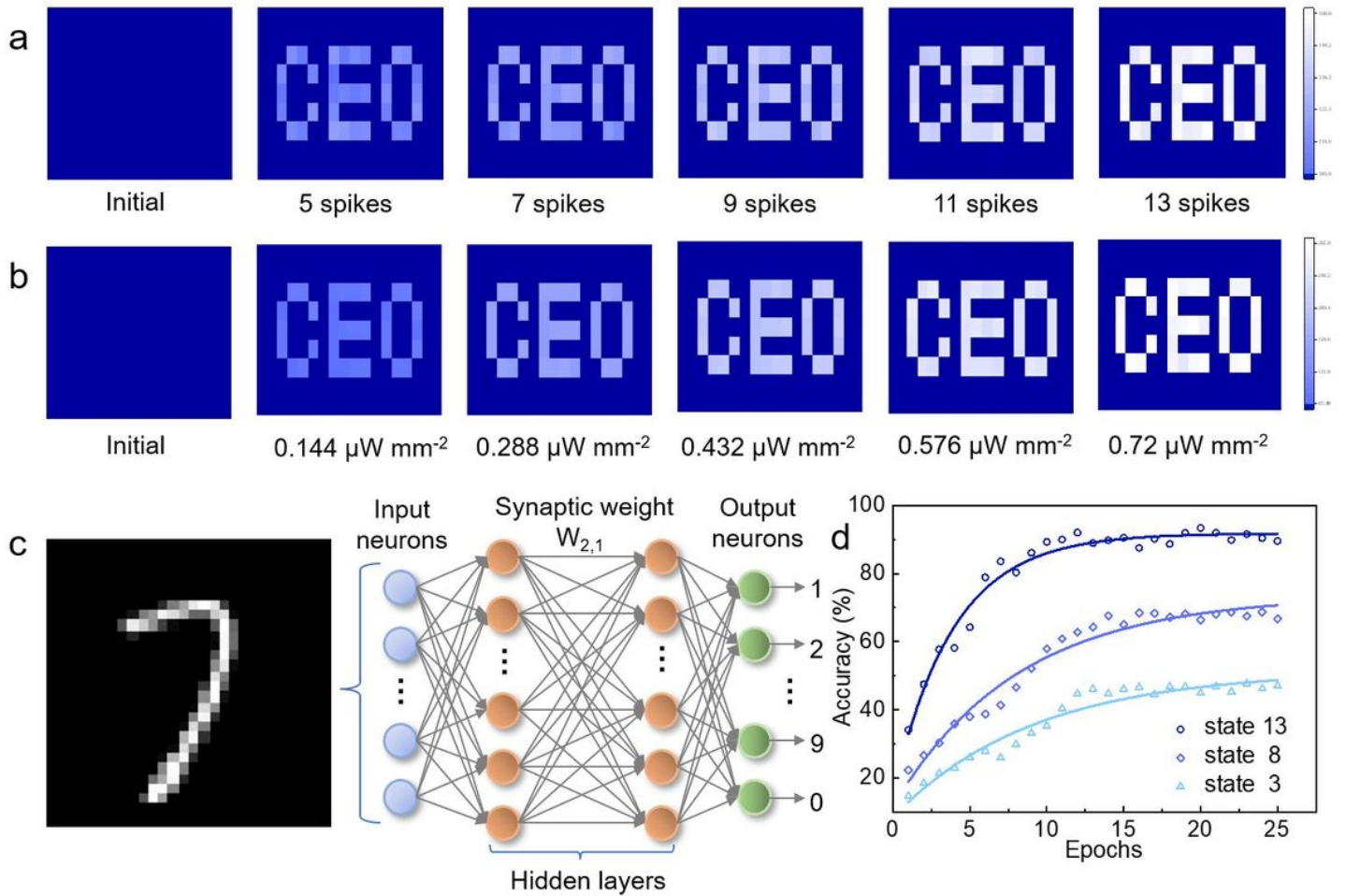


Figure 5

Image memorization and recognition. Measured weights of a 'CEO' pattern image in the initial state and a) after training with 5, 7, 9, 11, and 13 spikes under 365 nm light with a power density of $0.288 \mu\text{W mm}^{-2}$ (pulse width, 500 ms; pulse interval, 500 ms), b) after training with various power densities of 0.144, 0.288, 0.432, 0.576, and $0.72 \mu\text{W mm}^{-2}$ (pulse width, 500 ms; pulse interval, 500 ms) under 9 pulses at 365 nm. c) Schematic illustration of a light-derived neural network. d) Accuracy calculation of the network under different pulse states.

Supplementary Files

This is a list of supplementary files associated with this preprint. Click to download.

- [NCManuscriptSI.docx](#)